crystals

MDPI

Article

Synthesis and Optical Characterizations of Yb^{3+}: $Ca_xSr_{1-x}F_2$ Transparent Ceramics

Hongran Ling *, Bingchu Mei, Weiwei Li, Yu Yang, Yongqiang Zhang and Xinwen Liu

State Key Laboratory of Advanced Technology for Materials Synthesis and Processing, Wuhan University of Technology, Wuhan 430070, China; bcmeilab@163.com (B.M.); leeww0229@163.com (W.L.); yangyuwhut@163.com (Y.Y.); yongqiangzhang2021@163.com (Y.Z.); liuxinwen55@163.com (X.L.)
* Correspondence: 15155183801@163.com

Abstract: In this study, 3 at.% Yb^{3+}: $Ca_xSr_{1-x}F_2$ nanopowders were synthesized via the chemical co-precipitation method. Highly transparent 3 at.% Yb^{3+}: $Ca_xSr_{1-x}F_2$ ceramics with various CaF_2 concentrations were fabricated by hot-pressed sintering. The 3 at.% Yb^{3+}: $Ca_xSr_{1-x}F_2$ nanopowders exhibited a spherical shape with slight agglomeration, and their particle size ranged from 26 nm to 36 nm. With an increase of the CaF_2 concentration, the peak shape changed significantly and the width of the emission band increased inhomogeneously. The minimal fluorescence lifetime at the wavelength of 1011 nm of 3 at.% Yb^{3+}: $Ca_xSr_{1-x}F_2$ transparent ceramics with various CaF_2 concentrations was higher than 3.25 ms, which was longer than that of the 3 at.% Yb^{3+}: CaF_2 (2.6 ms) and the 3 at.% Yb^{3+}: SrF_2 (3.22 ms) reported in previous literature. The results indicate that incorporating Ca^{2+} ions into the SrF_2 is an effective method to modulate the optical properties of transparent ceramics.

Keywords: Yb^{3+}: $Ca_xSr_{1-x}F_2$; transparent ceramics; chemical co-precipitation; spectral property

Citation: Ling, H.; Mei, B.; Li, W.; Yang, Y.; Zhang, Y.; Liu, X. Synthesis and Optical Characterizations of Yb^{3+}: $Ca_xSr_{1-x}F_2$ Transparent Ceramics. *Crystals* **2021**, *11*, 652. https://doi.org/10.3390/cryst11060652

Academic Editors: Helmut Cölfen, Abel Moreno, Charles Rosenblatt, Sławomir Grabowski and Shujun Zhang

Received: 11 May 2021
Accepted: 5 June 2021
Published: 8 June 2021

1. Introduction

Since the first Dy: CaF_2 transparent ceramics were prepared by Hatch et al. in 1964 [1], alkaline-earth fluorides (AeF_2, Ae = Ca, Sr, Ba) have attracted much attention in the field of solid-state lasers because of their low phonon energy, high transmittance, and wide range of light transmission [2–4]. For instance, Su et al. prepared Tm^{3+}: CaF_2 single crystals and their slope efficiency reached up to 64.4%, which was higher than Tm^{3+}: YAG single crystals with 31.8% [5,6]. Basiev, T. T. et al. fabricated Nd^{3+}: SrF_2 laser ceramics with a laser slope efficiency of 19% [7]. On the other hand, AeF_2 possessed the cubic structure (F_{3m}^{m}) with fluoride ions occupying the centers of the octants and Ae^{2+} ions occupying the nodes in a face-centered lattice, which made it possible for the Re^{3+} (rare earth) ions to incorporate in the AeF_2 crystal structure and achieve high dopant concentrations. Moreover, various Re^{3+} ions have been successfully doped into alkaline earth fluorides, such as Nd^{3+}: CaF_2 crystals [8], Eu^{3+}: CaF_2 transparent ceramics [9], Er^{3+}: CaF_2 glass-ceramics [10], and Nd^{3+}: SrF_2 nanoparticles [11].

Among the Re^{3+} ions, Yb is one of the most promising elements for solid-state laser materials like high power or ultrafast lasers. Yb^{3+} ions possess a simple electronic-level structure with only two multiples $^2F_{7/2}$ and $^2F_{5/2}$, enabling efficient diode-pump laser systems [12–14]. A. Lucca et al. prepared the first diode-pumped laser based on the Yb^{3+}: CaF_2 single crystal and achieved a laser output of 5.8 W at 1053 nm [15]. Subsequently, a Yb^{3+}: CaF_2 single crystal achieved a 150 femtosecond, 880 mW laser output at the central wavelength of 1043 nm [16]. However, the local environment of Yb^{3+} ions affects its optical properties [17].

One of the effective methods to alter the local environment of Yb^{3+} ions is introducing non-active ions, like Ga^{3+} ions. Y.J. Wu and his co-workers modified their lattice structure by co-doping Ga^{3+} ions into Yb^{3+}: SrF_2 to form a disordered lattice site, broadening the

absorption and emission cross-sections, and explored the potential of the Yb^{3+}, Ga^{3+}: SrF_2 crystal in tunable and passively mode-locked lasers [18]. Further, due to the different radii of Ca^{2+} ions and Sr^{2+} ions, the local environment of rare earth ions in $Ca_xSr_{1-x}F_2$ ceramics varies with the concentration of CaF_2. Recently, a few studies have researched the CaF_2-SrF_2 mixed matrix because incorporating the Ca^{2+} ions into the SrF_2 destroys the symmetry of the crystal structure, thereby affecting its luminescence performance [19–21]. Compared with the Yb^{3+}: SrF_2 single crystal, the slope efficiency of CaF_2-SrF_2-YbF_3 nanoceramics is 1.7 times higher than the former [22]. Therefore, it is meaningful to investigate the influence of CaF_2 concentration on the optical properties of $Ca_xSr_{1-x}F_2$ transparent ceramics. However, according to the previous literature on $Ca_xSr_{1-x}F_2$ transparent ceramics, the ratio of SrF_2 to CaF_2 is relatively small [23]. When the proportion of SrF_2 is higher than 25 at.%, the Sr^{2+} cannot incorporate into the CaF_2 structure, and two single phases (CaF_2 and SrF_2) exist in the products [24]. In this paper, high purity of 3 at.% Yb^{3+}: $Ca_xSr_{1-x}F_2$ (x = 0.1, 0.3, 0.5, 0.7 and 0.9) nanopowders were synthesized via the coprecipitation method and the corresponding transparent ceramics were prepared by hot-pressed sintering. The morphology of 3 at.% Yb^{3+}: $Ca_xSr_{1-x}F_2$ nanopowders was observed by a scanning electron microscope (SEM). The optical quality, microstructure, and photoluminescence properties of 3 at.% Yb^{3+}: $Ca_xSr_{1-x}F_2$ transparent ceramics were also characterized and discussed.

2. Experimental Procedure

The 3 at.% Yb^{3+}: $Ca_xSr_{1-x}F_2$ (x = 0.1, 0.3, 0.5, 0.7 and 0.9) nanopowders were synthesized with the coprecipitation method by dropping the $KF{\cdot}2H_2O$ aqueous solution into the cationic aqueous solution ($Sr(NO_3)_2$, $Ca(NO_3)_2{\cdot}4H_2O$ and $Yb(NO_3)_3{\cdot}5H_2O$) under stirring. The 3 at.% Yb^{3+}: $Ca_xSr_{1-x}F_2$ nanopowders were prepared following this formulation:

$$0.03Yb(NO_3)_3 + xCa(NO_3)_2 + (1 - x)Sr(NO_3)_2 + 2.09KF \rightarrow Yb_{0.033}Ca_xSr_{1-x}F_{2.09}\downarrow + 2.09KNO_3$$

The obtained precipitates were aged for 3 h, and finally, the precipitates were washed with deionized water, filtered, and freeze-dried under vacuum for 8 h. The fully dried powder was ground in a mortar to remove large aggregates.

The 3 at.% Yb^{3+}: $Ca_xSr_{1-x}F_2$ transparent ceramics were fabricated by hot-pressing the as-synthesized nanopowders in vacuum. The nanopowders were calcined at 400 °C for 2 h to remove residual water and nitrates from the powder, then sintered at 800 °C under an axial pressure of 40 MPa for 2 h followed by cooling down to room temperature. Then, the 3 at.% Yb^{3+}: $Ca_xSr_{1-x}F_2$ transparent ceramics were both-side polished to 2 mm for further measurements.

The phase compositions of 3 at.% Yb: $Ca_xSr_{1-x}F_2$ ceramics were identified by X-ray diffraction (XRD, D8 Advance, Bruker, Karlsruhe, Germany). The morphology of nanopowders and the fracture microstructure of transparent ceramics of Yb^{3+}: $Ca_xSr_{1-x}F_2$ were observed by a scanning electron microscope (SEM, S4800, Hitachi, Tokyo, Japan). The average particle size of the Yb^{3+}: $Ca_xSr_{1-x}F_2$ transparent ceramic was calculated by scanning software. The in-line transmittance and absorption spectra of the Yb^{3+}: $Ca_xSr_{1-x}F_2$ transparent ceramics were measured by a spectrophotometer (U-3500, Hitachi, Tokyo, Japan). The photoluminescence (PL) spectra and fluorescence lifetimes were recorded by a spectrofluorometer (FLS980, Edinburgh, Livingston, UK) at room temperature.

3. Results and Discussion

The XRD patterns of 3 at.% Yb^{3+}: $Ca_xSr_{1-x}F_2$ transparent ceramics with various CaF_2 concentrations and standard XRD patterns of CaF_2 (JCPDS file number 65-0535) and SrF_2 (JCPDS file number 06-0262) are shown in Figure 1a. All the diffraction peaks of 3 at.% Yb: $Ca_xSr_{1-x}F_2$ transparent ceramics corresponded well to the cubic CaF_2 and/or SrF_2 phase without redundant peaks. With the increase of CaF_2 concentration, the position of all diffraction peaks shifted to a high angle, and was closer to the peak of pure CaF_2, indicating that the position of Sr^{2+} ions was replaced by the Ca^{2+} ions in the SrF_2 unit cell and formed a solid solution structure instead of a two-phase composite structure of CaF_2 and SrF_2.

According to the Hume-Rothery solid solution theory, taking r_1 and r_2 to represent the ionic radius of different ions, there is the empirical formula [25]

$$\Delta r = \left| \frac{r_1 - r_2}{r_1} \right|$$

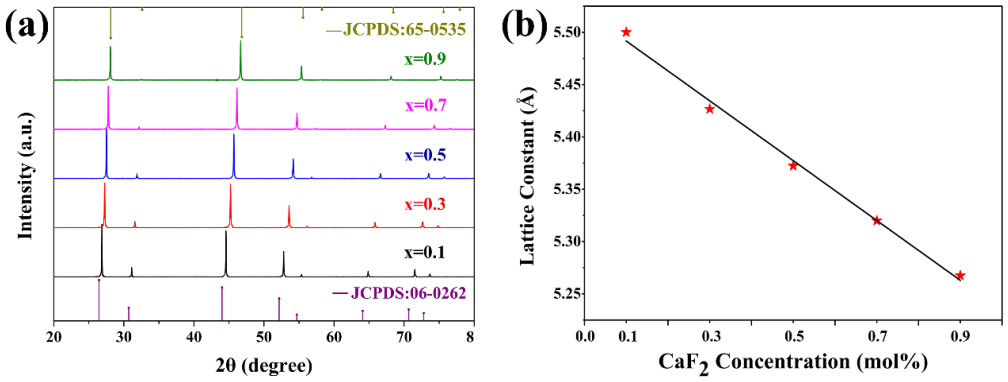

Figure 1. (**a**) XRD patterns of 3 at.% Yb^{3+}: $Ca_xSr_{1-x}F_2$ (x = 0.1, 0.3, 0.5, 0.7 and 0.9) transparent ceramics and (**b**) lattice constant as a function of CaF_2 concentration.

According to the formula, the obtained value of Δr was 10%. Further, the two ions had the same valence state and CaF_2 and SrF_2 possess the same fluorite structure. Therefore, Ca^{2+} ions can be incorporated into the SrF_2 unit cell at any ratio to form a continuous solid solution instead of destroying the unit cell structure. In addition, the lattice constant of Yb^{3+}: $Ca_xSr_{1-x}F_2$ was calculated by the Barrage equation and is presented in Figure 1b. At lower CaF_2 concentrations, the lattice constant was close to that of SrF_2, while at higher CaF_2 concentrations, the lattice constant was close to that of CaF_2. The linear relationship between the lattice constant and CaF_2 concentration was corresponded well to the 2θ shift trend in Figure 1b. In the condition of the expansion of the lattice constant when larger Sr^{2+} ions were substituted, the stability of the unit cell structure was still maintained.

The SEM images of 3 at.% Yb^{3+}: $Ca_xSr_{1-x}F_2$ (x = 0.1, 0.3, 0.5, 0.7 and 0.9) nanopowders are shown in Figure 2. All 3 at.% Yb^{3+}: $Ca_xSr_{1-x}F_2$ nanopowders exhibited a spherical shape and uniform distribution in the field of vision with slight agglomeration. With the increase of the CaF_2 concentration, there was nearly no significant change in the shape and particle size of the powder. The average particle size of the powders ranged from 26 nm to 34 nm.

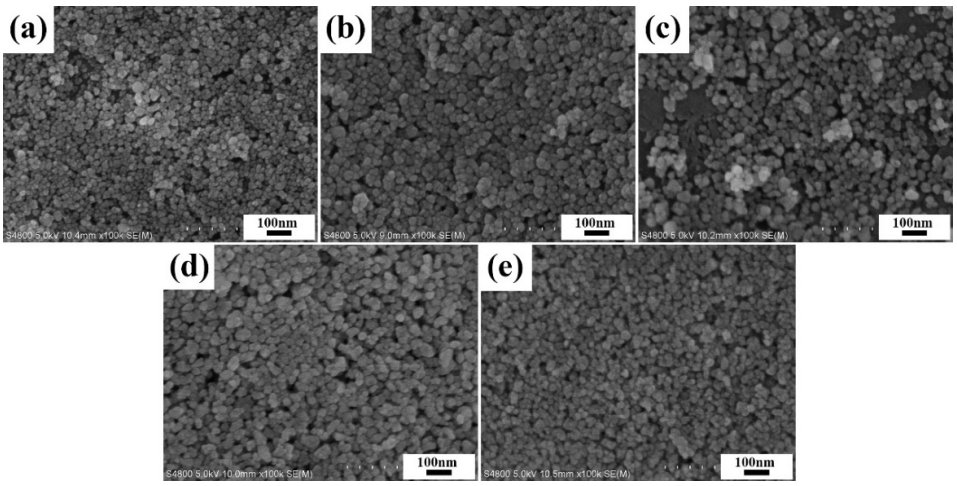

Figure 2. SEM images of 3 at.% Yb^{3+}: $Ca_xSr_{1-x}F_2$ nanopowders with various CaF_2 concentrations: (**a**) x = 0.1, (**b**) x = 0.3, (**c**) x = 0.5, (**d**) x = 0.7, and (**e**) x = 0.9.

The in-line transmittance spectra and photographs of as-fabricated 3 at.% Yb^{3+}: $Ca_xSr_{1-x}F_2$ (x = 0.1, 0.3, 0.5, 0.7 and 0.9) transparent ceramics are presented in Figure 3. The 3 at.% Yb^{3+}: $Ca_{0.5}Sr_{0.5}F_2$ transparent ceramics had the highest optical transmittance among the five samples. The text on the paper can be clearly identified through the ceramics. The transmittance of all ceramics was higher than 80% over the wavelength of 1130 nm and reached 90% around 2000 nm, which might be attributed to the well-dispersed nanopowders. The small and spherical-shaped nanopowders had relatively large surface energy and high sintering activity, which was favorable for the sintering process. In addition, well dispersion of the nanopowders was conducive to the discharge of pores. However, the incorporation of CaF_2 caused the lattice distortion of the matrix material, which affected the sintering activity of the synthesized nanopowders. Then, the diffusion rate of the powder was affected by the nanopowders which obsess different sintering activity, resulting in different pores in the sample. At ultraviolet wavelength range, the 3 at.% Yb^{3+}: $Ca_{0.5}Sr_{0.5}F_2$ transparent ceramic possessed the highest in-line transmittance, which might have been caused by the absence of impurities and fewer micropores in the ceramic. However, a significant transmittance loss was observed at the ultraviolet wavelength range similar to the CaF_2 and SrF_2 transparent ceramics [26,27], which might have been caused by fewer micro-obturator pores existing in the sample. When the size of the scattering source was much smaller than the wavelength of the incident light, the scattering intensity and the incident light wavelength conformed to Rayleigh's law of scattering [28]:

$$S = \left(128\pi^5 d^6/3\lambda^4\right)\left\{\left[\left(\frac{n_2}{n_1}\right)^2 - 1\right]/\left[\left(\frac{n_2}{n_1}\right)^2 - 2\right]\right\}^2$$

where S, d, λ, and n_2 and n_1 are the cross section for the scattering of a particle, the radius of the scattering body, the measuring wavelength, and the refractive indexes for the host materials and scattering body, respectively. According to Rayleigh's law of scattering, scattering intensity is inversely proportional to the fourth power of the wavelength of the incident light. Therefore, the micropores inside the ceramic strongly led to the scatter of short-wavelength light such as ultraviolet light, which affected the transmittance of transparent ceramics in the ultraviolet wavelength range.

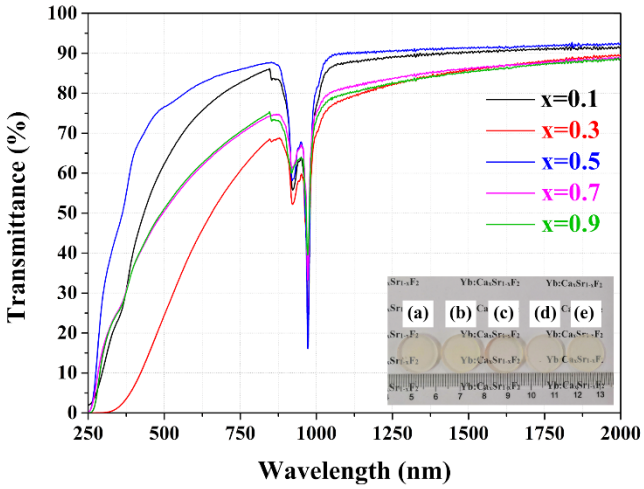

Figure 3. In-line transmittance spectra of as-fabricated 3 at.% Yb^{3+}: $Ca_xSr_{1-x}F_2$ (x = 0.1, 0.3, 0.5, 0.7 and 0.9) transparent ceramics, and insert shows the appearance of ceramics with the thickness of 2 mm.

As can be seen in SEM micrographs of the fracture surface of 3 at.% Yb^{3+}: $Ca_xSr_{1-x}F_2$ transparent ceramics (Figure 4), at a low CaF_2 concentration (x = 0.1, 0.3), transgranular fractures accounted for a large proportion. With an increase of the CaF_2 concentration, the transgranular fractures gradually decreased and tended to disappear, and intergranular

fractures were the main fracture mode. Intracrystalline pores can affect the fracture mode of ceramic samples. It can be clearly seen that there were some intracrystalline pores inside the ceramics when the CaF_2 concentration was low. The intracrystalline pores were the starting point of the crack propagation during the fracture process, which extended to the grain boundary to form transgranular fractures. When the intracrystalline pores gradually decreased, the proportion of transgranular fractures also decreased.

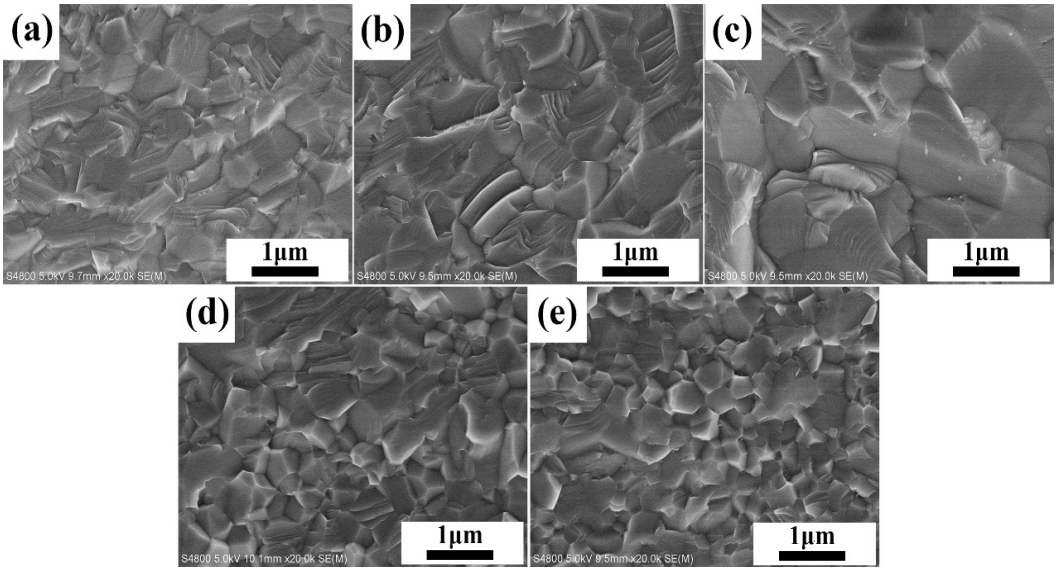

Figure 4. SEM micrographs of the fracture surface of 3 at.% Yb^{3+}: $Ca_xSr_{1-x}F_2$ transparent ceramics: (**a**) x = 0.1, (**b**) x = 0.3, (**c**) x = 0.5, (**d**) x = 0.7 and (**e**) x = 0.9.

Figure 5 shows the relative absorption (divide intensity by Yb concentration) spectra of 3 at.% Yb^{3+}: $Ca_xSr_{1-x}F_2$ (x = 0.1, 0.3, 0.5, 0.7 and 0.9) transparent ceramics. The absorption spectra of all samples possessed a similar shape with two absorption peaks, located at 922 nm and 972 nm, respectively. This was caused by the stark split of ground state $^2F_{7/2}$ energy levels and the excited state $^2F_{5/2}$ energy levels. In general, the absorption intensity increased with an increase of the Yb^{3+} concentration. Considering the influence of the Yb^{3+} concentration on the absorption intensity, we conducted an ICP test (within ±0.01 margin of error) to determine the practical doping concentration of $Yb^{3+,}$ and have attached the test result in Table 1. The test result was consistent with the result of the absorption spectrum. Thus, we attributed the change in absorption intensity to the change in the practical doping concentration of Yb^{3+}.

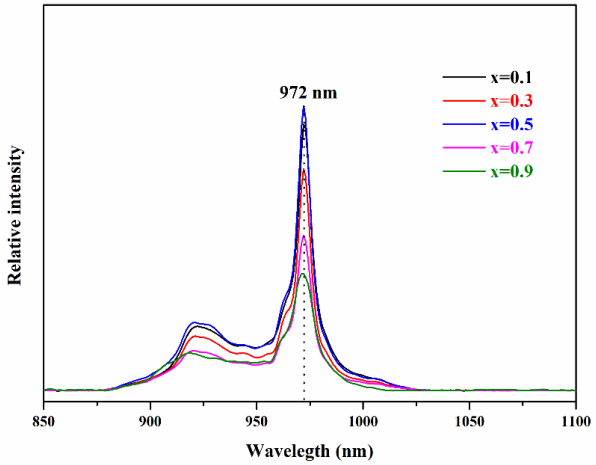

Figure 5. Absorption spectra of 3 at.% Yb^{3+}: $Ca_xSr_{1-x}F_2$ (x = 0.1, 0.3, 0.5, 0.7 and 0.9) transparent ceramics.

Table 1. Designed concentration and practical concentration of Yb^{3+} in 3 at.% Yb^{3+}: $Ca_xSr_{1-x}F_2$ (x = 0.1, 0.3, 0.5, 0.7 and 0.9) transparent ceramics.

Sample	Yb^{3+} (mol%)	
	Designed Value	ICP Result (±0.01)
3 at.% Yb: $Ca_{0.1}Sr_{0.9}F_2$	3	2.82
3 at.% Yb: $Ca_{0.3}Sr_{0.7}F_2$	3	2.67
3 at.% Yb: $Ca_{0.5}Sr_{0.5}F_2$	3	2.84
3 at.% Yb: $Ca_{0.7}Sr_{0.3}F_2$	3	2.63
3 at.% Yb: $Ca_{0.9}Sr_{0.1}F_2$	3	2.60

The emission spectra of the 3 at.% Yb^{3+}: $Ca_xSr_{1-x}F_2$ transparent ceramics with different concentrations of CaF_2 (x = 0.1, 0.3, 0.5, 0.7 and 0.9) are shown in Figure 6. With the increase of CaF_2 concentrations, the peak shape changed significantly and the width of the emission band increased inhomogeneously. It can be seen in Figure 6 that there were three different emission peaks located at 976 nm, 1011 nm and 1027 nm, respectively. The intensity of the emission peaks at 976 nm and 1011 nm gradually increased with the increase of the CaF_2 concentration. The emission peak at 1027 became much clearer when the CaF_2 concentration was higher than 0.7, which might be attributed to the tendency of Yb^{3+} ions in the AeF_2 matrix to form different centers of symmetry. With the increase of the cation radius (Ca → Sr → Ba), the symmetric system gradually changed from C_{4v} to C_{3v}. The emission peak of the tetragonal symmetry center of Yb^{3+} in AF_2 (A = Ca, Sr) was located at 1025 nm [29]. Therefore, when the concentration of CaF_2 increased, the proportion of the symmetry center of C_{4v} gradually increased, and the emission peak near 1027 became much clearer. Further, Youngman et al. have proved that the substitution of Ca^{2+} ions for Sr^{2+} ions is random in $Ca_{1-x}Sr_xF_2$ single crystals [30]. Similarly, the linear relationship in Figure 1b proved that it also conformed to Vegard's law in $Ca_xSr_{1-x}F_2$ transparent ceramics. The substitution of Ca^{2+} ions in $Ca_xSr_{1-x}F_2$ transparent ceramics is random, too [31]. Therefore, on the one hand, when Ca^{2+} ions replaced Sr^{2+} ions, the distance between Yb^{3+} decreased, leading to an increase in the degree of clustering of Yb^{3+}. A wealth of lattice sites formed, combining the Yb^{3+} cluster with different symmetry, resulting in the broadening of the spectrum. On the other hand, the substitution process caused lattice distortion and affected the Yb^{3+} crystal field environment. The combined effect of the two aspects caused the inhomogeneous broadening of the emission spectrum [24].

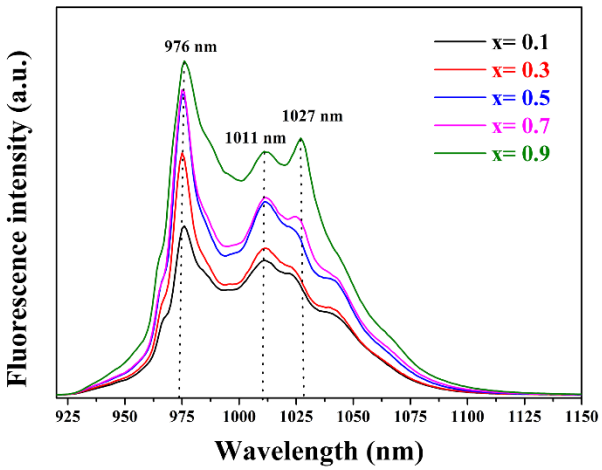

Figure 6. Emission spectra of the 3 at.% Yb^{3+}: $Ca_xSr_{1-x}F_2$ (x = 0.1, 0.3, 0.5, 0.7 and 0.9) transparent ceramics.

The room-temperature luminescence decay curves of 3% at. Yb^{3+}: $Ca_xSr_{1-x}F_2$, with different concentrations of CaF_2 (x = 0.1, 0.3, 0.5, 0.7 and 0.9) at 976 nm and 1011 nm pumped by the xenon lamp of 896 nm, are shown in Figure 7a,b, respectively. To visualize

the change of lifetime with the concentration of CaF_2, the change curve of the fluorescence lifetime at 976 nm and 1011 nm as a function of the CaF_2 concentration is presented in Figure 8. A single exponential function was used to fit the decay curve of all ceramics:

$$I(t) = A1\exp(-t/\tau 1) + I0$$

where I(t) and I_0 represent the luminescence intensity at time t and t_0, respectively; t is time; A_1 is a constant; τ_1 is the decay time.

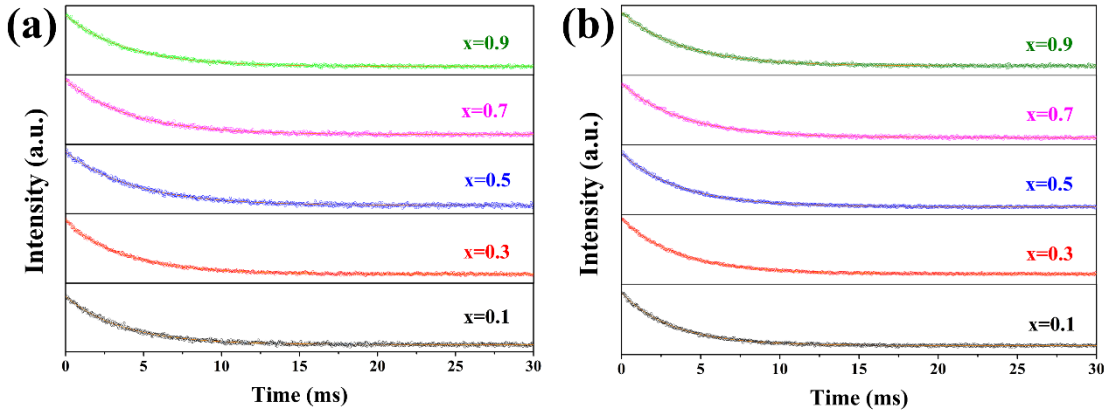

Figure 7. Luminescence decay curves at (**a**) 976 nm and (**b**) at 1011 nm of 3 at.% Yb^{3+}: $Ca_xSr_{1-x}F_2$ (x = 0.1, 0.3, 0.5, 0.7 and 0.9) transparent ceramics with various CaF_2 concentrations.

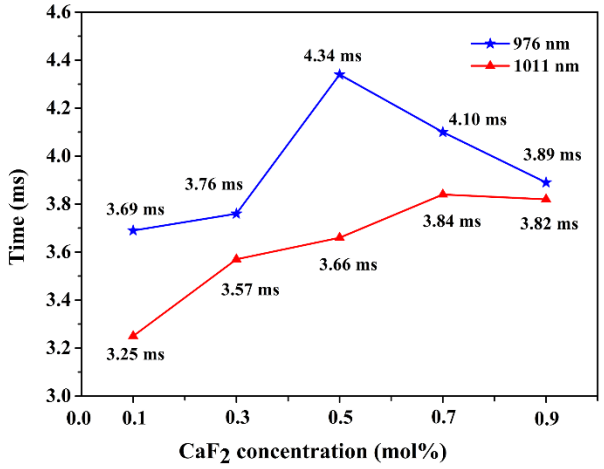

Figure 8. Luminescence lifetime curves of 3 at.% Yb^{3+}: $Ca_xSr_{1-x}F_2$ (x = 0.1, 0.3, 0.5, 0.7 and 0.9) transparent ceramics with various CaF_2 concentrations.

The fluorescence lifetime at 976 nm gradually increased from 3.69 ms to 4.34 ms and then decreased to 3.89 ms with the increase of the CaF_2 concentration. Similarly, the fluorescence lifetime at 1011 nm increased from 3.25 ms to 3.84 ms and then decreased to 3.82 ms (the fluorescence lifetime value is the average value of the four test results). The fluorescence lifetime at 976 nm was longer than that at 1011 nm, which may have been caused by the re-absorption at 976 nm. This is because there was an overlap area between the absorption peak at 972 nm and the emission peak at 976 nm. Therefore, when Yb^{3+}: $Ca_xSr_{1-x}F_2$ transparent ceramics were excited by the 896 nm xenon lamp to emit 976 nm light, this wavelength was in the absorption band, so it was reabsorbed. Similarly, there was no reabsorption at 1011 nm because Yb^{3+}: $Ca_xSr_{1-x}F_2$ transparent ceramics have extremely weak absorption at 1011 nm. Moreover, compared with Yb^{3+}: CaF_2 [32] (about 2.6 ms) and Yb^{3+}: SrF_2 [33] (about 3.22 ms), the fluorescence lifetime of Yb^{3+}: $Ca_xSr_{1-x}F_2$ with the same rare earth doping concentration was longer than both of them. This can

be attributed to the incorporation of CaF_2. On the one hand, the incorporation of Ca^{2+} broke the clusters of Yb^{3+} ions, thereby increasing the fluorescence lifetime. On the other hand, when the doping ratio was higher, the crystal lattice tended to be CaF_2, and the fluorescence lifetime of Yb^{3+}: CaF_2 transparent ceramics were lower than that of Yb^{3+}: SrF_2 transparent ceramics, so the fluorescence lifetime was reduced. Under the combined effect of two factors, the fluorescence lifetime of Yb^{3+}: $Ca_xSr_{1-x}F_2$ transparent ceramics presented a curve that first increased and then decreased.

4. Conclusions

Highly pure 3 at.% Yb^{3+}: $Ca_xSr_{1-x}F_2$ (x = 0.1, 0.3, 0.5, 0.7 and 0.9) nanopowders with various CaF_2 concentrations were successfully synthesized by the chemical co-precipitation method. The phase analysis showed that CaF_2 can be incorporated into the crystal lattice of SrF_2 at any ratio. With an increase of the CaF_2 concentration, the lattice constant of 3 at.% Yb^{3+}: $Ca_xSr_{1-x}F_2$ decreased. All the as-fabricated 3 at.% Yb^{3+}: $Ca_xSr_{1-x}F_2$ transparent ceramics possessed high optical quality, with their in-line transmittance higher than 80% at the wavelength of 1130 nm. The absorption spectra of all 3 at.% Yb^{3+}: $Ca_xSr_{1-x}F_2$ transparent ceramics samples had similar spectra shapes. With the increase of CaF_2 concentrations, the peak shape changed significantly and the width of the emission bands gradually increased. The fluorescence lifetime of all 3 at.% Yb^{3+}: $Ca_xSr_{1-x}F_2$ transparent ceramics at 1011 nm exceeded 3.25 ms, which is suitable for high-power laser output. Above all, incorporating Ca^{2+} ions into the SrF_2 is an effective method to modulate the optical properties of transparent ceramics. The present results can stimulate further studies on the modulation of optical spectra and the performance of solid-state laser materials.

Author Contributions: H.L. and B.M. conceived this research and experimental plan. H.L. conducted experiments and wrote the first draft of the paper. W.L., Y.Y., Y.Z., X.L. reviewed and edited the manuscript. All authors have read and agreed to the published version of the manuscript.

Funding: This research was funded by National Natural Science Foundation of China, grant number No: 51972245.

Conflicts of Interest: The authors declare that they have no conflict of interest to this work. We declare that we do not have any commercial or associative interest that represents a conflict of interest in connection with the work submitted.

References

1. Hatch, S.E.; Parsons, W.F.; Weagley, R.J. Hot pressed polycrystalline CaF_2: Dy ceramic lasers. *Appl. Phys. Lett.* **1964**, *5*, 153–154. [CrossRef]
2. Srivastava, R.; Lauer, H.; Chase, L.; Bron, W. Raman frequencies of fluorite crystals. *Phys. Lett.* **1971**, *36A*, 333–334. [CrossRef]
3. Rubloff, G.W. Far-ultraviolet reflectance spectra and the electronic structure of ionic crystals. *Phys. Rev.* **1972**, *B5*, 662–684. [CrossRef]
4. Lyberis, A.; Patriarche, G.; Gredin, P.; Vivien, D.; Mortier, M. Origin of light scattering in ytterbium doped calcium fluoride transparent ceramic for high power lasers. *J. Eur. Ceram. Soc.* **2011**, *31*, 1619–1630. [CrossRef]
5. Wang, Y.; Wang, S.; Wang, J.; Zhang, Z.; Zhang, Z.; Liu, R.; Zu, Y.; Liu, J.; Su, L. High-efficiency ~2 μm CW laser operation of LD-pumped Tm^{3+}: CaF_2 single-crystal fibers. *Opt. Expreess* **2020**, *28*, 6684–6695. [CrossRef]
6. Jinge, L.; Ya, W.; Shuo, L.; Liangyu, G.; Chunting, W.; Yongji, Y.; Chao, W.; Guangyong, J. Study on LD end-pumped multi-segment bonded Tm: YAG solid-state laser. *Opt. Commun.* **2021**, *480*, 126452. [CrossRef]
7. Basiev, T.T.; Doroshenko, M.E.; Konyushkin, V.A.; Osiko, V.V. SrF_2: Nd^{3+} laser fluoride ceramics. *Opt Lett.* **2010**, *35*, 4009–4011. [CrossRef] [PubMed]
8. Alimov, O.K.; Basiev, T.T.; Doroshenko, M.E.; Fedorow, P.P.; Konyushkin, V.A.; Nakladov, A.N.; Osiko, V.V. Investigation of Nd^{3+} ions spectroscopic and laser properties in SrF_2 fluoride single crystal. *Opt Mater.* **2012**, *34*, 799–802. [CrossRef]
9. Samuel, P.; Ishizawa, H.; Ezura, Y.; Ueda, K.I.; Babu, S.M. Spectroscopic analysis of Eu doped transparent CaF_2 ceramics at different concentration. *Opt. Mater.* **2011**, *33*, 735–737. [CrossRef]
10. Fan, J.; Chen, S.; Yuan, X.; Jiang, Y.; Pan, L.; Jiang, B.; Mao, X.; Li, R.; Jiang, X.; Zhang, L. Recrystallization of Er^{3+}: CaF_2 in Transparent Fluorophosphate Glass-Ceramics with the Co-Firing Method. *J. Am. Ceram. Soc.* **2016**, *99*, 2971–2976. [CrossRef]
11. Zhou, Z.W.; Li, W.W.; Song, J.H.; Yi, G.; Mei, B.; Su, L. Synthesis and characterization of Nd^{3+} doped SrF_2 nanoparticles prepared by precipitation method. *Ceram. Int.* **2018**, *44*, 4344–4350. [CrossRef]

12. Lu, X.; Jiang, B.; Li, J.; Liu, W.; Wang, L.; Ba, X.; Hu, C.; Liu, B.; Pan, Y. Synthesis of highly sinterable Yb: Sc_2O_3 nanopowders for transparent ceramic. *Ceram. Int.* **2013**, *39*, 4695–4700. [CrossRef]
13. Zhang, L.; Pan, W.; Feng, J. Dependence of spectroscopic and thermal properties on concentration and temperature for Yb: Y_2O_3 transparent ceramics. *J. Eur. Ceram. Soc.* **2015**, *35*, 2547–2554. [CrossRef]
14. Takaichi, K.; Yagi, H.; Shirakawa, A.; Ueda, K.; Hosokawa, S.; Yanagitani, T.; Kaminskii, A.A. Lu_2O_3:Yb^{3+} ceramics-a novel gain material for high-power solid-state lasers. *Phys. Status. Solidi A* **2005**, *202*, 1–3. [CrossRef]
15. Lucca, A.; Jacquemet, M.; Druon, F.; Balembois, F.; Georges, P.; Camy, P.; Doualan, J.L.; Moncorgé, R. High-power tunable diode-pumped Yb^{3+}: CaF_2 laser. *Opt. Lett.* **2004**, *29*, 1879–1881. [CrossRef]
16. Lucca, A.; Debourg, G.; Jacquemet, M.; Druon, F.; Balembois, F.; Georges, P.; Camy, P.; Doualan, J.L.; Moncorgé, R. High-power diode-pumped Yb^{3+}: CaF_2 femtosecond laser. *Opt. Lett.* **2004**, *29*, 2767–2769. [CrossRef]
17. Petit, V.; Camy, P.; Doualan, J.-L. Spectroscopy of Yb^{3+}: CaF_2: From isolated centers to clusters. *Phys. Rev. B.* **2008**, *78*, 085131. [CrossRef]
18. Wu, Y.; Zou, Z.; Wang, C.; Liu, J.; Zheng, L.; Su, L. Broadly tunable and passively mode-locked operations of Yb^{3+}, Gd^{3+}: SrF_2 Laser. *IEEE J. Sel. Top. Quant.* **2019**, *25*, 1100405. [CrossRef]
19. Jiang, Y.G.; Wang, Z.Y.; Zhang, L.F.; Yuan, C.; Zhang, L. Transparent Nd, Y- Codoped $Ca_{1-x}Sr_xF_2$ glass-ceramic with large emission bandwidth tailored by a controllable spontaneous precipitation under supersaturated state. *Ceram. Int.* **2019**, *45*, 24651–24655. [CrossRef]
20. Veselský, K.; Šulc, J.; Jelínková, H.; E Doroshenko, M.; A Konyushkin, V.; Nakladov, A.N. Spectroscopic and laser properties of a broadly tunable diode-pumped Tm^{3+}: CaF_2-SrF_2 laser. *Laser Phys. Lett.* **2020**, *17*, 025802. [CrossRef]
21. Tian, X.Q.; Ma, F.K.; Zhang, Z. Linear correlation of crystal structure and spectral properties of Nd^{3+} in $Ca_{1-x}Sr_xF_2$ mixed crystals. *J. Am. Ceram. Soc.* **2020**, *103*, 3650–3656. [CrossRef]
22. Basiev, T.T.; Doroshenko, M.E.; Fedorov, P.P.; Konyushkin, V.A.; Kuznetsov, S.; Osiko, V.V.; Akchurin, M.S. Efficient laser based on CaF_2-SrF_2-YbF_3 nanoceramics. *Opt. Lett.* **2008**, *33*, 521–523. [CrossRef] [PubMed]
23. Zhu, C.; Song, J.; Mei, B.; Li, W.; Liu, Z. Fabrication and optical characterizations of CaF_2-SrF_2-NdF_3 transparent ceramic. *Mater. Lett.* **2016**, *167*, 115–117. [CrossRef]
24. Zhou, Z.; Mei, B.; Song, J.; Li, W.; Yang, Y.; Yi, G. Effects of Sr^{2+} content on microstructure and spectroscopic properties of Nd^{3+} doped $Ca_{1-x}Sr_xF_2$ transparent ceramics. *J. Alloy Compd.* **2019**, *811*, 152046. [CrossRef]
25. Hume-Rothery, W. Comments on papers resulting from Hume-Rothery´s Note-1965. *Acta Metall.* **1967**, *15*, 567–569. [CrossRef]
26. Wan, Z.; Li, W.; Mei, B.; Liu, Z.; Yang, Y. Fabrication and spectral properties of Ho-doped calcium fluoride transparent ceramics. *J. Lumin.* **2020**, *223*, 117188. [CrossRef]
27. Xiong, F.; Song, J.; Li, W.; Mei, B.; Su, L. Influence of sintering conditions on the microstructure and optical properties of Eu: CaF_2 transparent ceramic. *Mater. Res. Bull.* **2017**, *95*, 138–145. [CrossRef]
28. Ikesue, A.; Yoshida, K.; Yamamoto, T.; Yamaga, I. Optical scattering centers in polycrystalline Nd: YAG laser. *J. Am. Ceram. Soc.* **1997**, *80*, 1517–1522. [CrossRef]
29. Aidilibike, T.; Guo, J.; Li, Y.; Liu, X.; Qin, W. Triplet cooperative luminescence of Yb^{3+}-doped AF_2 (A=Ca, Sr) crystals. *J. Lumin.* **2017**, *188*, 107–111. [CrossRef]
30. Youngman, R.E.; Smith, C.M. Multinuclear NMR studies of mixed $Ca_{1-x}Sr_xF_2$ crystals. *Phys. Rev. B* **2008**, *78*, 014112. [CrossRef]
31. Vegard, L. Die konstitution der mischkristalle und die raumfellung der atome. *Z. Phys.* **1921**, *5*, 17–26. [CrossRef]
32. Lyberis, A.; Stevenson, A.J.; Suganuma, A.; Ricaud, S.; Druon, F.; Herbst, F.; Vivien, D.; Gredin, P.; Mortier, M. Effect of Yb^{3+} concentration on optical properties of Yb: CaF_2 transparent ceramics. *Opt. Mater.* **2012**, *34*, 965–968. [CrossRef]
33. Gao, Y.W.; Mei, B.C.; Li, W.W.; Zhou, Z.; Liu, Z. Effect of Yb^{3+} concentration on microstructure and optical properties of Yb: SrF_2 transparent ceramics. *Opt. Mater.* **2020**, *105*, 109869. [CrossRef]